Supplementary Information for "Optimizing the Performance of Aerosol Photoacoustic Cells using a Finite Element Model. Part 2: Application to a Two-Resonator Cell"

Michael I. Cotterell,[1,2] Gareth P. Ward,[3] Alastair P. Hibbins,[3] Andy Wilson,[2] Jim M. Haywood[1,2] and Justin M. Langridge[2]

[1]College for Engineering, Mathematics and Physical Sciences, University of Exeter, Exeter, EX4 4QF, United Kingdom.

[2]Observation Based Research, Met Office, Exeter, EX1 3PB, United Kingdom.

[3]Electromagnetic and Acoustic Materials Group, Department of Physics and Astronomy, University of Exeter, Exeter, EX4 4QF, United Kingdom.

Author for correspondence: m.cotterell@exeter.ac.uk

S1. Impact of mirror symmetry boundary conditions on the identified number of pressure eigenmodes

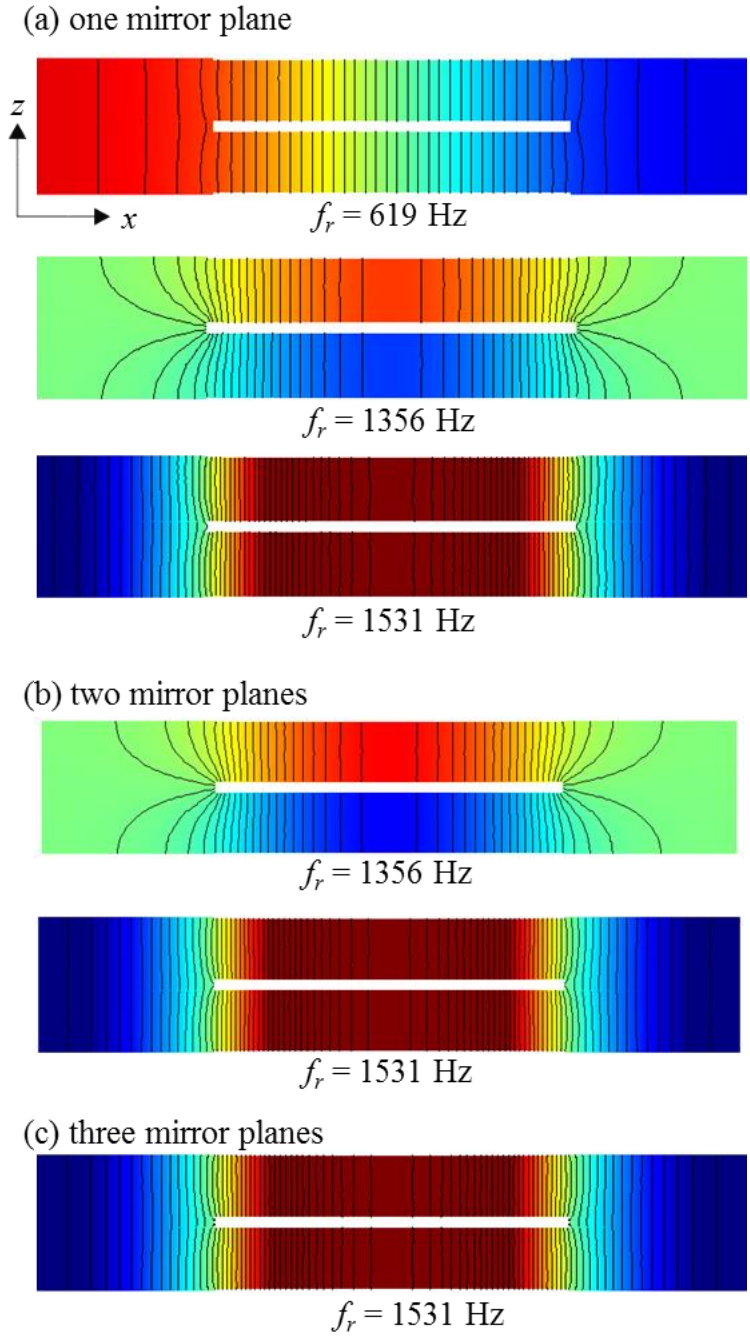

Figure S1. Pressure eigenmodes for a two-resonator PA cell without window volumes to increase symmetry such that three mirror symmetry planes bisect the geometry. Symmetry planes exist in the *z*-*x* plane (plane of the page), in the *z*-*y* plane bisecting both resonator centres and one in the *y*-*x* plane between the two separate resonators. Figure S1(a) shows the eigenmodes found by COMSOL when only the *z*-*x* mirror plane is used to define symmetry boundary conditions, Figure S1(b) shows the located eigenmodes when both *z*-*x* and *z*-*y* mirror symmetry boundary conditions are used, while Figure S1(c) shows the located eigenmodes when all three mirror symmetry boundary conditions are used. When mirror symmetry boundary conditions are applied, some eigenmodes fail to be identified in COMSOL. For example, upon increasing the symmetry in going from (a) to (b), the mode at f_r = 619 Hz is not identified because this mode involves a change in phase that is antisymmetric about the *z*-*y* mirror plane and therefore is forbidden by imposing the *z*-*y* mirror symmetry boundary conditions.

S2. The flat-window two-resonator PA cell: understanding the frequency dependence in the microphone responses for window heating

Figure S2(a) shows line profiles of the ring and longitudinal pressure eigenmodes along the *x*-axis through the centres of the upper and lower resonator. The heating domains mimicking laser-window interactions are located at the *x*-axis extremes (at the window volume boundaries) on the lower resonator axis, corresponding to $x = \pm 12$ cm. At these locations, the pressure eigenmode amplitudes ($p_n(\vec{r}_{win})$) for the ring and longitudinal modes are 0.098 Pa and 5.789 Pa respectively, i.e. the overlap integral of the window acoustic pressure source with the $n = 3$ (longitudinal) eigenmode wavefunction is 59 times larger than for the corresponding overlap integral with the $n = 2$ (ring) eigenmode.

Although the longitudinal eigenfrequency is separated by ~150 Hz from that of the ring mode, coupling into the longitudinal mode has significant influence on the pressure response at the ring mode eigenfrequency. Here, we use an empirical model consistent with equation 2 in the main text to understand the frequency-dependent pressure response at the microphone positions resulting from window heating $|p^{bck}(\vec{r}_M, \omega)|$ as a sum of Lorentzian distributions, with a contribution from each *n* pressure eigenmode:

$$|p^{bck}(\vec{r}_M, \omega)| = \sum_{n=1}^{N} \varphi_n(\vec{r}_M) \left(\frac{[p_n(\vec{r}_{win}) p_n(\vec{r}_M)]^2}{1 + \left(2Q_n \frac{(f - f_n)}{f_n}\right)^2} \right)^{0.5} \quad \text{(S1)}$$

in which $\varphi_n(\vec{r}_M)$ is the phase of the pressure eigenmode at the microphone location, $p_n(\vec{r}_{win})$ is the pressure eigenmode amplitude at the location of the window heating volumes and $p_n(\vec{r}_M)$ is the pressure eigenmode amplitude at the location of the microphone. Here, we consider only the contributions from the ring and longitudinal modes. We take $Q_n = 100$ for both eigenmodes, $f_2 = 1355$ Hz, $f_3 = 1502$ Hz, $p_n(\vec{r}_{win})$ takes the aforementioned values of $p_2(\vec{r}_{win}) = 0.098$ Pa and $p_3(\vec{r}_{win}) = 5.789$ Pa, and the phases take values $\varphi_2(\vec{r}_{M,up}) = -1$, $\varphi_2(\vec{r}_{M,low}) = +1$, $\varphi_3(\vec{r}_{M,up}) = \varphi_3(\vec{r}_{M,low}) = -1$. From the eigenmode simulations (Figure 3(a) in the main text), $p_2(\vec{r}_M)$ and $p_3(\vec{r}_M)$ were taken as 12.4 Pa and 10.1 Pa, respectively, for microphones in both the upper and lower resonators. Using this empirical expression for $|p^{bck}(\vec{r}_M, \omega)|$, Figure S2(b) plots the frequency-dependent $|p^{bck}(\vec{r}_M, \omega)|$ predicted for the microphones in the upper resonator, lower resonator and for the differential amplifier response. Furthermore, the figures show component contributions to the total response from coupling into the two eigenmodes.

For window heating, longitudinal mode excitation makes a larger contribution to the individual microphone responses than excitation of the ring mode. $\left|p^{bck}(\vec{r}_M, \omega)\right|$ from our empirical model shows similar non-symmetric variation with frequency about the ring mode eigenfrequency as found in our FEM simulation results (Figure 4(b) of main text). Importantly, the longitudinal mode contribution is mostly subtracted out by passing the individual microphone responses through a differential amplifier because the longitudinal eigenmode phase in the two resonators are near-equal. Meanwhile, the ring mode contribution is amplified by the differential amplifier due to the opposite phases in the two resonators. Therefore, the differential amplifier response in the frequency domain is described well by a single Lorentzian distribution associated with detection of only ring mode excitation.

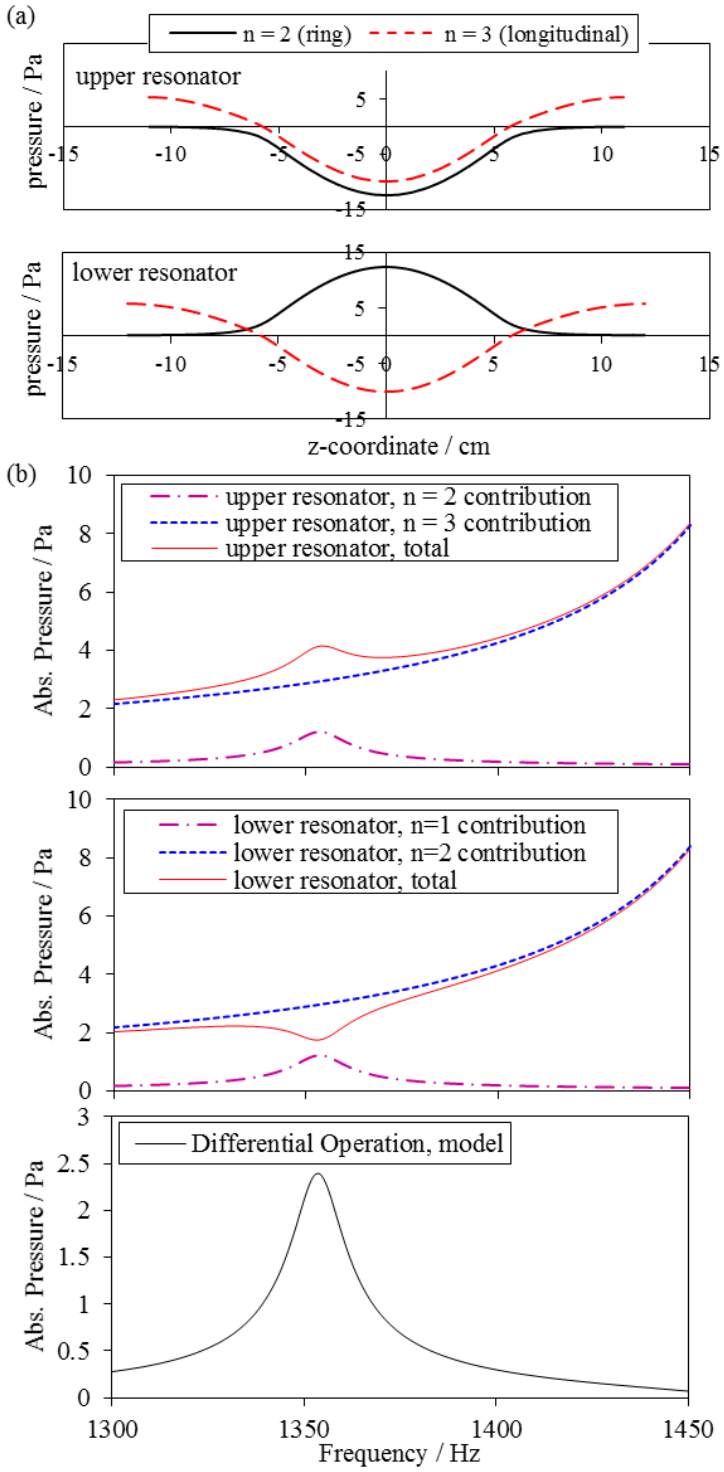

Figure S2. Line profiles of the acoustic pressure along the horizontal *z*-axis through the centre of each resonator, for the n = 2, 3 eigenmodes. (b) Empirical model calculations of the frequency-dependent pressure magnitude at the microphone locations resulting from window heating. We show the model responses in the upper resonator, lower resonator and for differential operation. These plots also show the individual contributions from excitation of the n = 2 and n = 3 eigenmodes in addition to the total response.

S3. Understanding the behaviour of the two-resonator cell with Brewster-angled windows

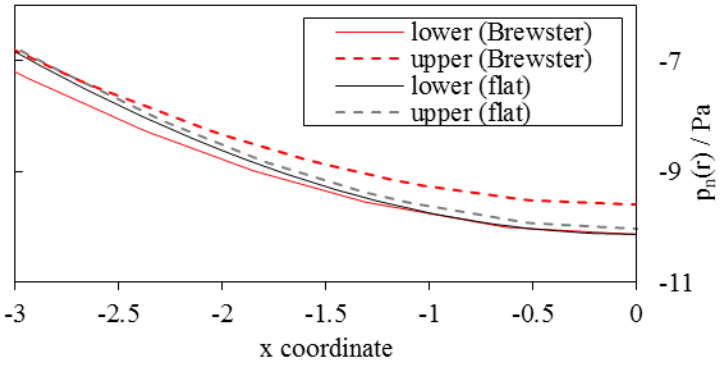

Figure S3. An expanded portion of n = 3 (longitudinal) mode line profiles through the upper and lower resonator centres of the two-resonator PA cells with either flat or Brewster-angled windows. The microphones are located at x = 0.

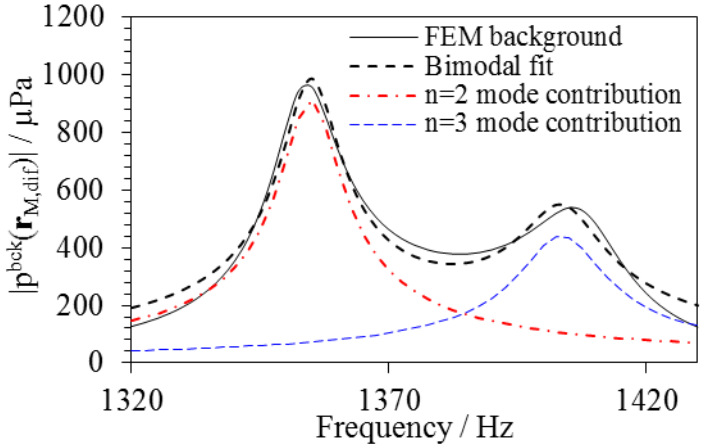

Figure S4. Comparison of the FEM predicted $|p^{bck}(\vec{r}_{M,dif})|$ to a best-fit bimodal Lorentzian distribution. Also shown are the individual contributions of n = 2 and n = 3 mode excitation to the total best-fit response.

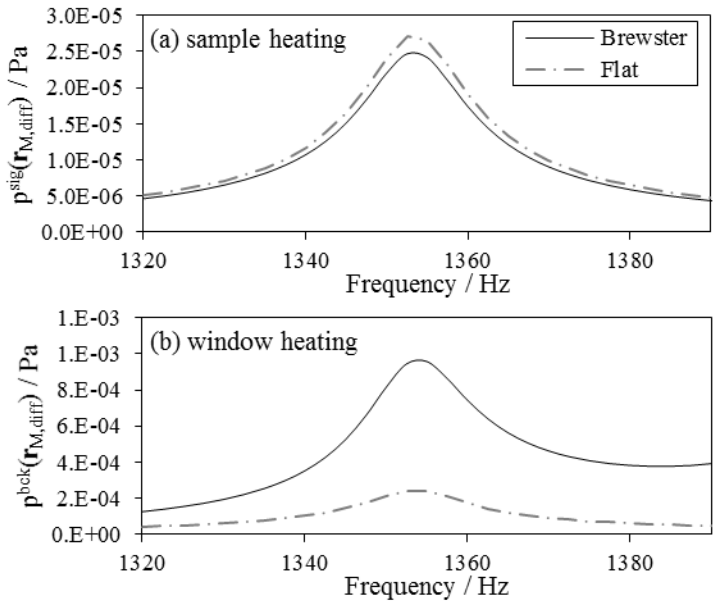

Figure S5. Comparison of frequency-dependent pressure response for PA cells with either Brewster or flat windows. Cases are presented for acoustic excitation by: (a) sample heating; (b) window heating.

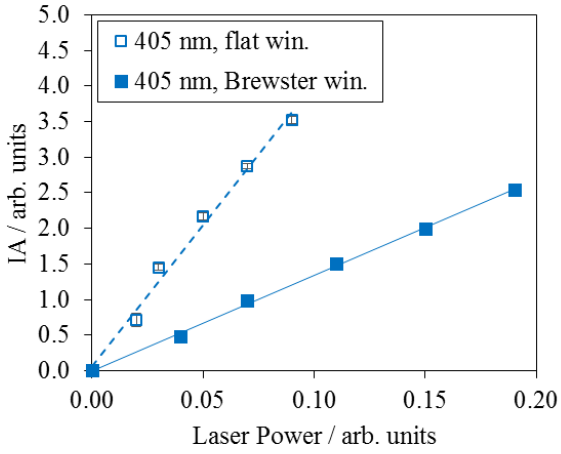

Figure S6. Experimental measurements of the background (window heating) photoacoustic response (IA) with variation in laser power for our two-resonator PA cell with either flat or Brewster-angled windows, with laser excitation performed at a 405 nm wavelength.

S4. Supplementary plots for Sect. 4.3.2. Optimising the height and width of the buffer volume

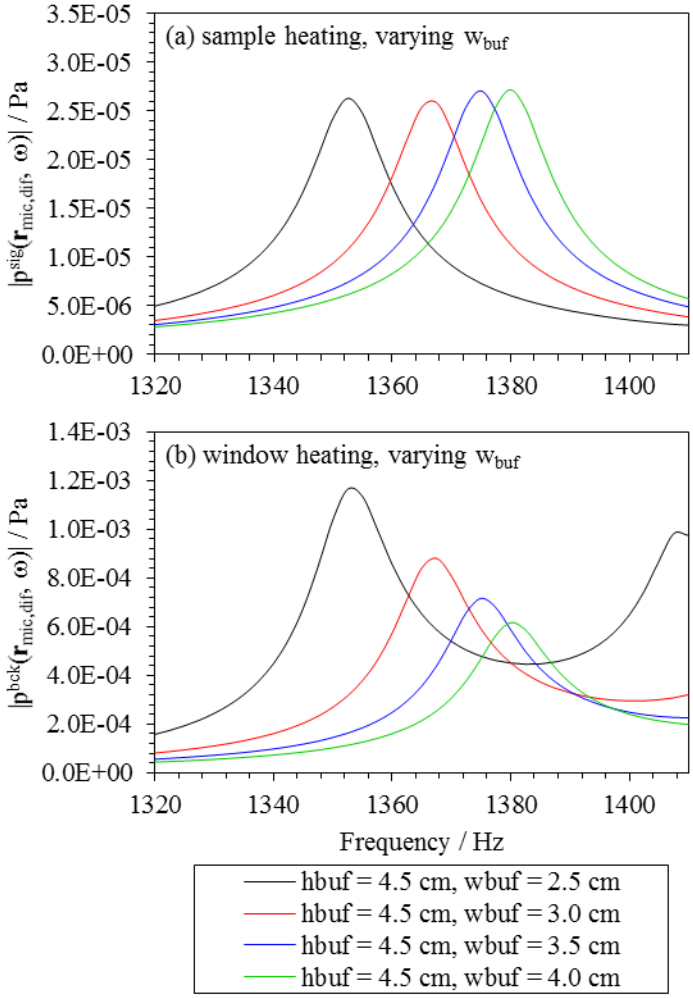

Figure S7. FEM predictions of frequency-dependent microphone response (differential operation) for the two-resonator PA cell with variation in w_{buf} for cases of (a) sample heating, and (b) window heating. w_{buf} is varied over the range 2.5 – 4.0 cm in 0.5 cm steps, while h_{buf} was kept constant at 4.5 cm.

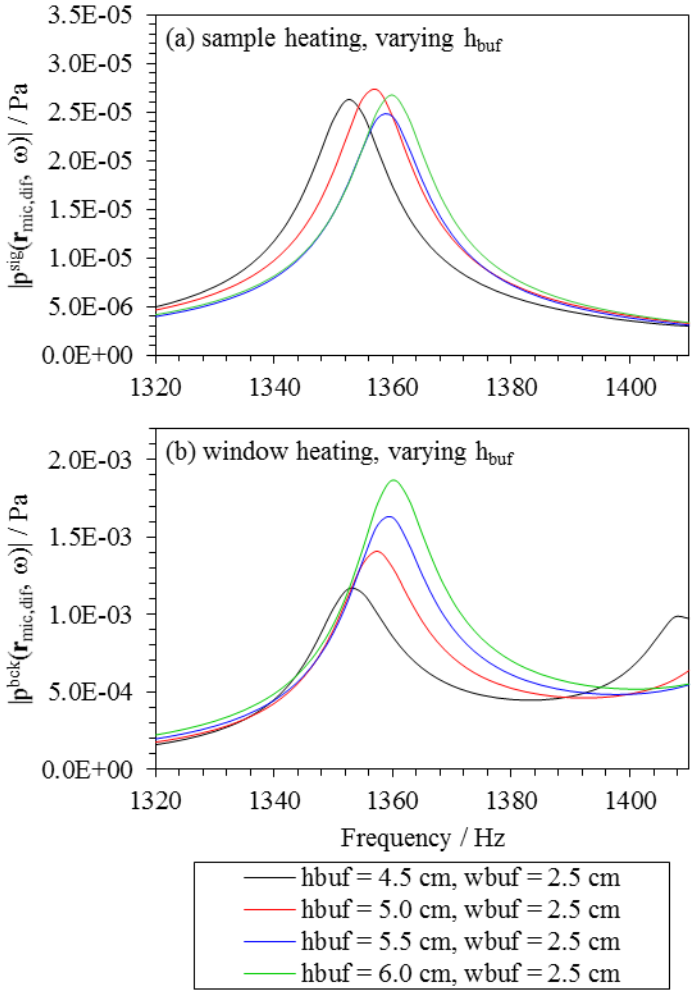

Figure S8. FEM predictions of frequency-dependent microphone response (differential operation) for the two-resonator PA cell with variation in h_{buf} for cases of (a) sample heating, and (b) window heating. h_{buf} is varied over the range 4.5 – 6.0 cm in 0.5 cm steps, while w_{buf} was kept constant at 2.5 cm.

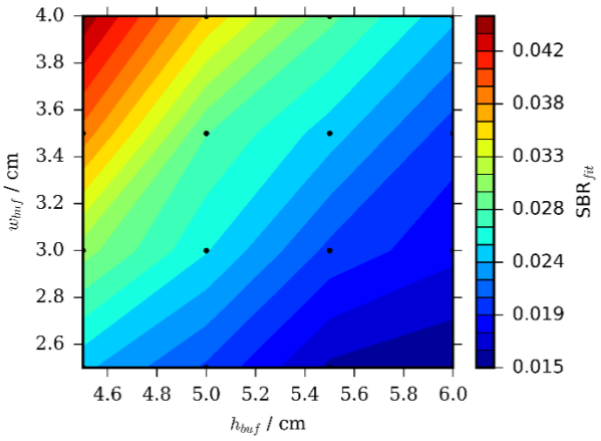

Figure S9. A contour plot to show the variation in SBR with parametric variation in h_{buf} from 4.5 to 6.0 cm in 0.5 cm steps and w_{buf} from 2.5 cm to 4.0 cm in 0.5 cm steps. The black points indicate the discrete value pairs of {h_{buf}, w_{buf}} input to simulations.

S5. Supplementary plots for Sect. 4.3.3. Optimising the fillet radius of the buffer volume

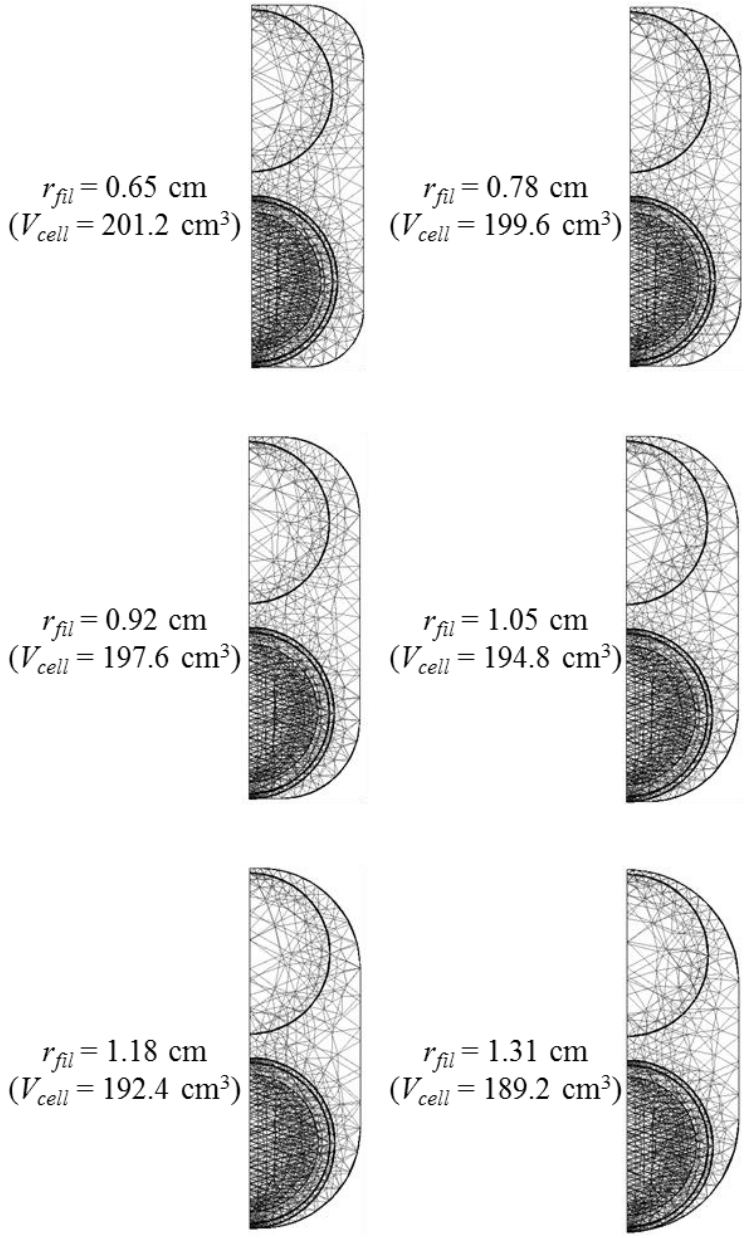

Figure S10. Cross sections through the PA cell buffer volume showing the changing buffer fillet radius r_{fil} used in FEM simulations. The cross sections show the element mesh used. The variation in the PA cell volume V_{cell} is indicated for each r_{fil}.

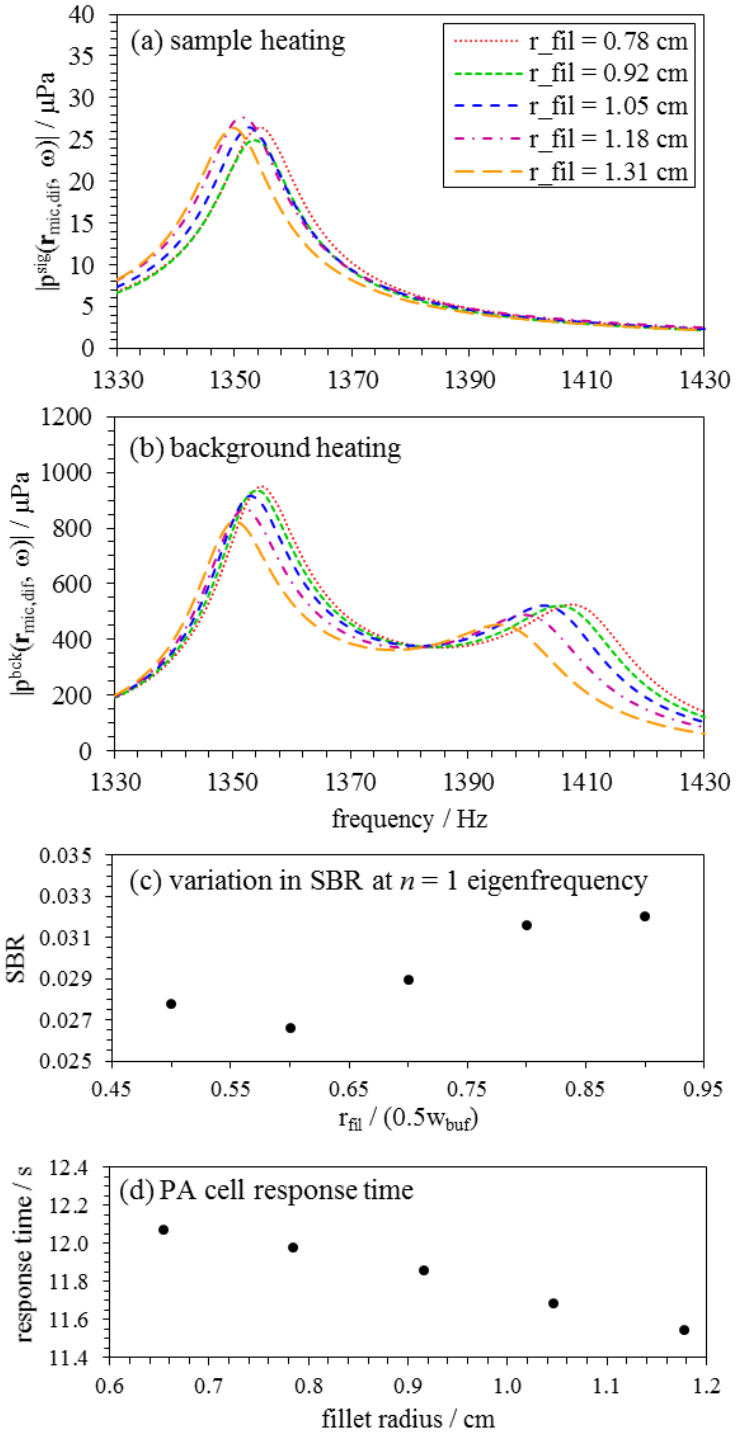

Figure S11. FEM simulations of the frequency-dependent (a) $|p^{sig}(\vec{r}_{M,dif}, \omega)|$, and (b) $|p^{bck}(\vec{r}_{M,dif}, \omega)|$ for the two-resonator PA cell with varying buffer fillet radius, r_{fil}. (c) The SBR calculated from the ratio of the sample and window heating responses at the ring mode eigenfrequency. (d) The PA cell response time calculated from the total PA cell volume and assuming a sample flow rate of 1.0 L min^{-1}.

S6. Supplementary plots for Sect. 4.3.4. Optimising the upper resonator radius ($r_{res,up}$) and the resonator separation distance (d_{res})

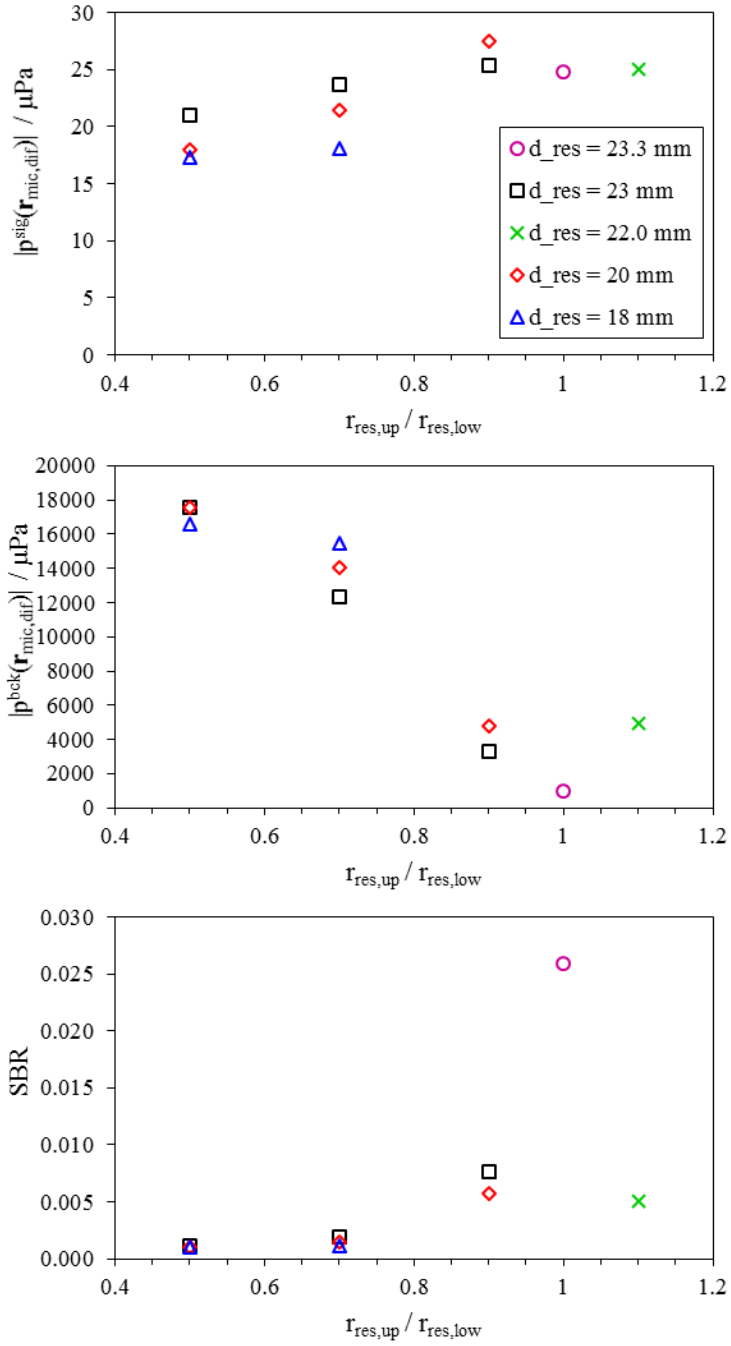

Figure S12. For variation in $r_{res,up}$ (x-axis) and d_{sep} (different data series), the differential microphone response at the ring mode eigenfrequency for (a) sample heating $|p^{sig}(\vec{r}_{M,dif})|$, (b) window heating $|p^{bck}(\vec{r}_{M,dif})|$, and (c) SBR.

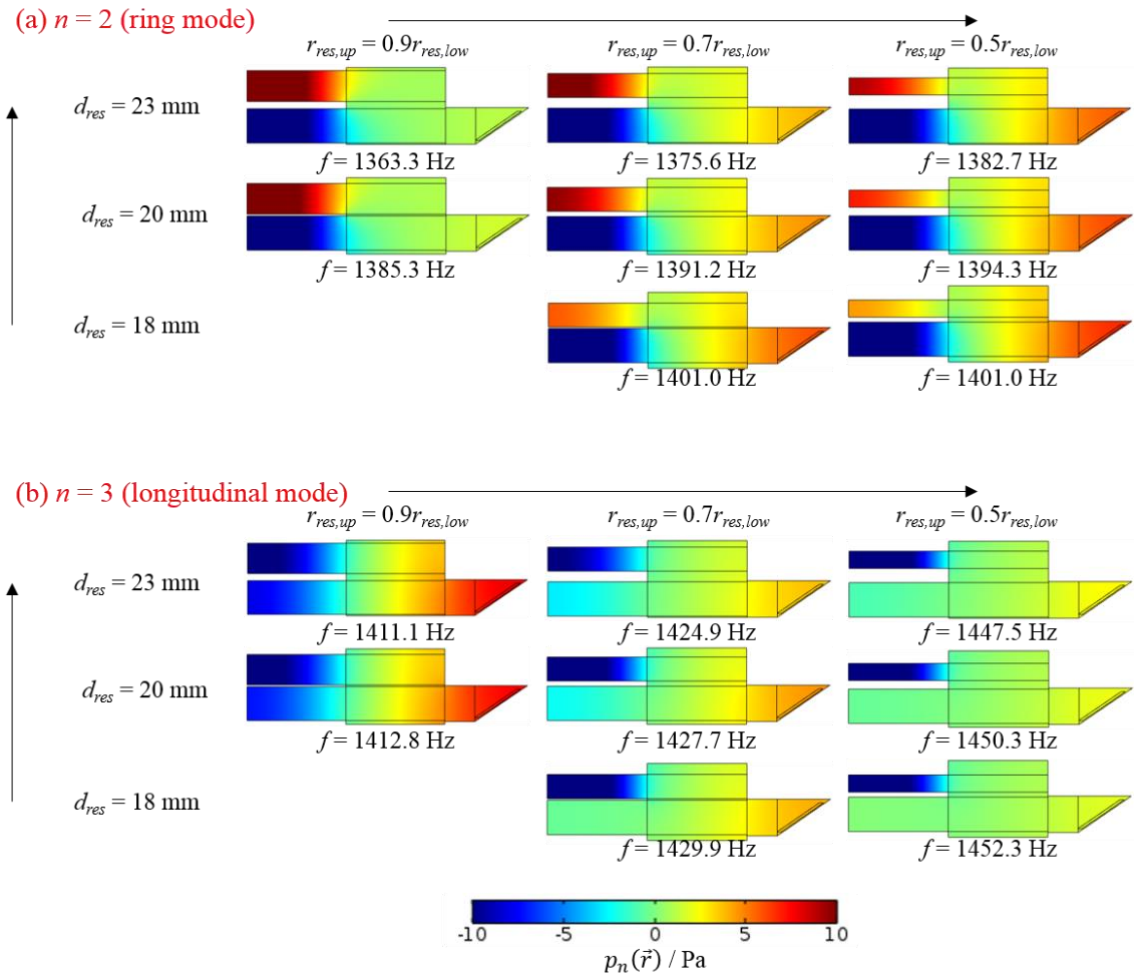

Figure S13. The ring and longitudinal eigenmode pressure distributions from simulations of the thermoviscous acoustic fields for the two-resonator PA cell with variation in the upper resonator radius ($r_{res,up}$) and the centre-to-centre resonator separation (d_{res}).

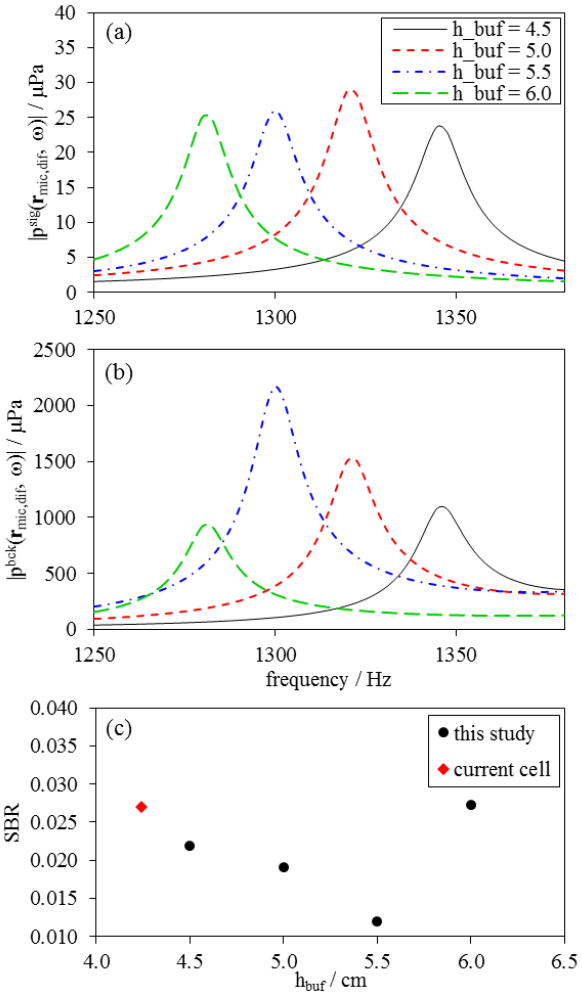

Figure S14. For the two-resonator cell, FEM predictions of the frequency-dependent differential microphone response for (a) sample heating, and (b) window heating for different h_{buf}, with d_{res} set to its maximum value. (c) The predicted variation in SBR with h_{buf} (with d_{res} set to its maximum value), also showing the predicted SBR for the current cell geometry (h_{buf} = 4.2 cm).

S7. Supplementary plots for Sect. 4.3.6. Optimising the buffer and resonator lengths for a conserved total cell length

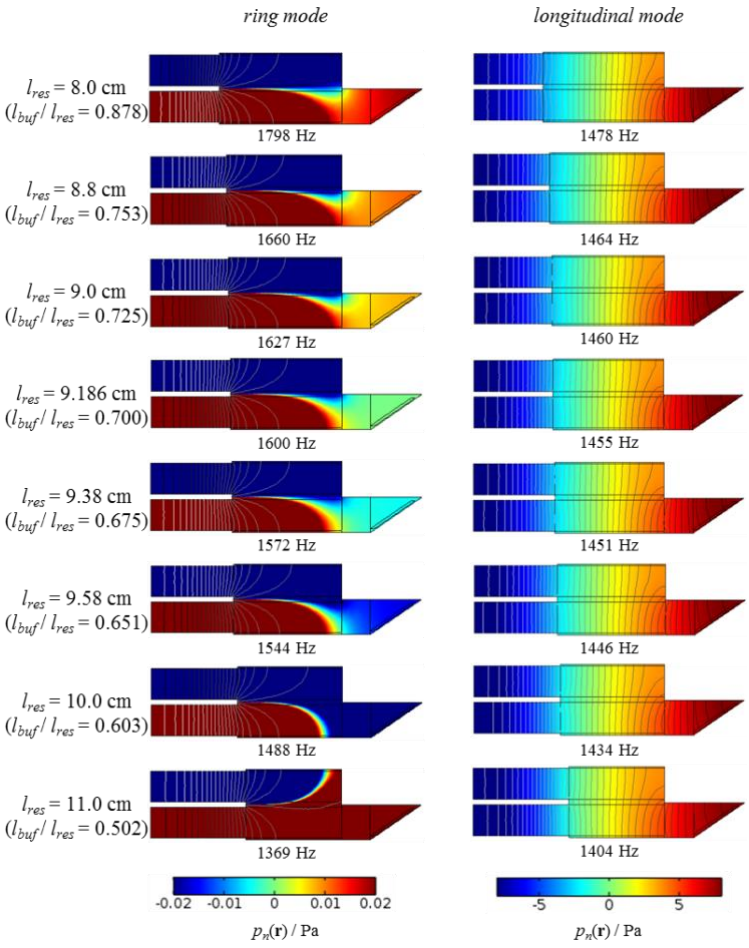

Figure S15. FEM predictions of the eigenmode pressure distributions $p_n(\vec{r})$ for the ring and longitudinal modes for a candidate cell with varying l_{buf}/l_{res} ratio, with l_{buf}/l_{res} varying from 0.88 to 0.50. The spatial distributions in $p_n(\vec{r})$ are shown on colour scales to highlight interesting features of either the ring or longitudinal mode.

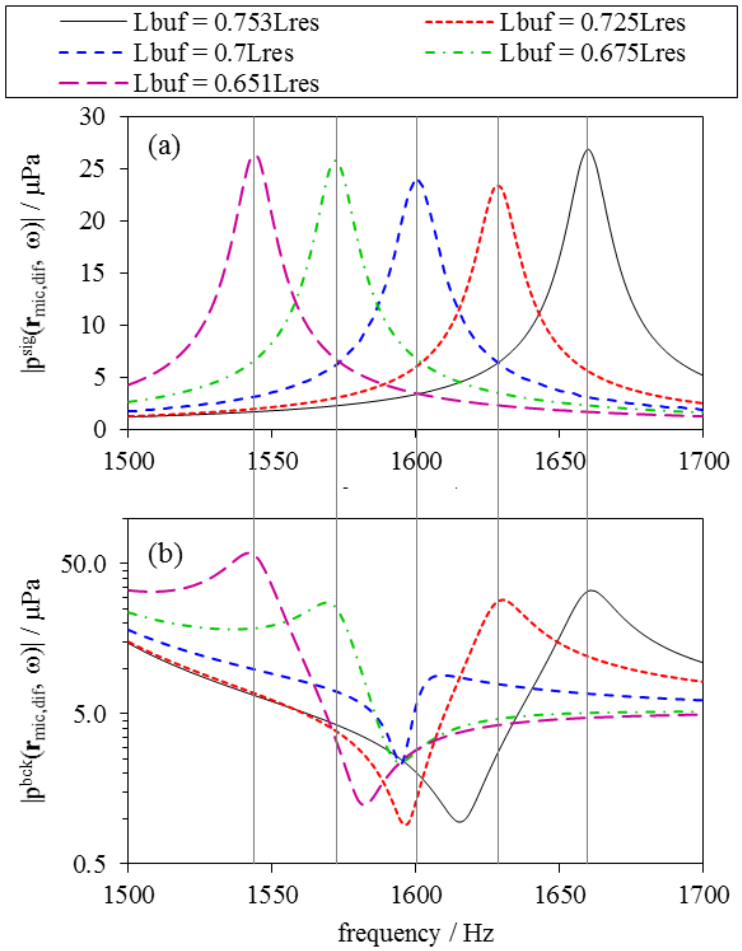

Figure S16. For the candidate cell, FEM predictions of (a) $|p^{sig}(\vec{r}_{M,dif}, \omega)|$ (sample heating) and (b) $|p^{bck}(\vec{r}_{M,dif}, \omega)|$ (window heating) for l_{buf}/l_{res} values of 0.651, 0.675, 0.700, 0.725 and 0.753. The vertical lines indicate the ring mode eigenfrequencies demarked by the frequency locations of the sample heating maxima in (a).

S8. Supplementary plots for Sect. 4.4. An optimised two-resonator PA cell: model vs measurement

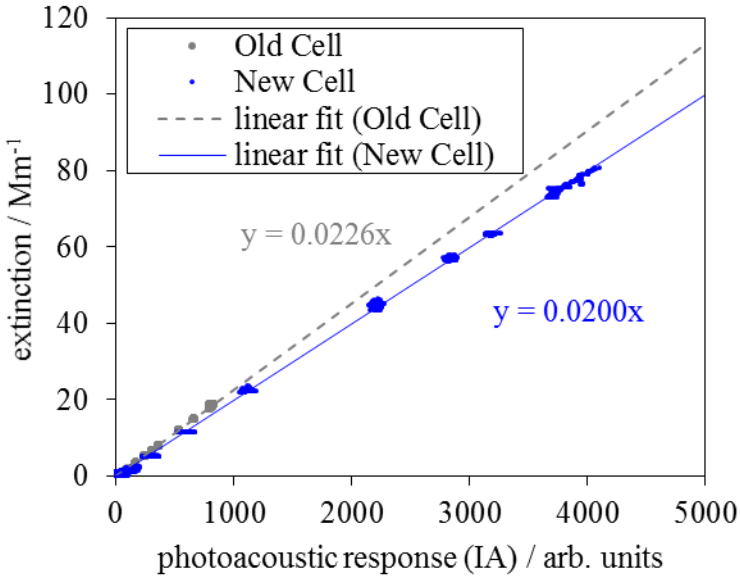

Figure S17. For measurements using either the original or optimised photoacoustic cell, example calibration measurements of the relationship between PAS response and the absorption coefficient for an ozone-laden air sample as determined using cavity ring-down spectroscopy. The lines represent linear regressions to the measured data, with the fit constrained such that the intercept is zero. The slopes of these linear regressions are labelled.